Porous Transport Layers for Proton Exchange Membrane Electrolysis under Extreme Conditions of Current Density, Temperature and Pressure

S. Stiber[1], H. Balzer[2], A. Wierhake[2], F. J. Wirkert[3], J. Roth[3], U. Rost[3,†], M. Brodmann[3], J. K. Lee[4], A. Bazylak[4], W. Waiblinger[1], A. S. Gago[1,*], K. A. Friedrich[1,5]

[1]*Institute of Technical Thermodynamics / Electrochemical Energy Technology German Aerospace Center (DLR) Pfaffenwaldring 38-40, 70569 Stuttgart, Germany.*

[2]*GKN Sinter Metals Filters GmbH, Dahlienstraße 43, 42477 Radevormwald, Germany.*

[3]*Westfälische Hochschule University of Applied Sciences, Neidenburger Str. 43, 45897 Gelsenkirchen, Germany.*

[4]*Department of Mechanical and Industrial Engineering, Faculty of Applied Science and Engineering, University of Toronto Institute for Sustainable Energy, University of Toronto, Toronto Ontario, M5S 3G8, Canada.*

[5]*Institute for Building Energetics, Thermotechnology and Energy Storage, University of Stuttgart, Stuttgart, 70550, Germany.*

*Corresponding author: Tel.: +49 711 6862-8090, fax: +49 711 6862-747, e-mail address: aldo.gago@dlr.de (A. S. Gago).

[†]Present address: ProPuls GmbH. Neidenburger Str. 10, 45897 Gelsenkirchen.

Keywords

PEM electrolysis; Porous Transport Layer; High Current Density; High Temperature; High Pressure

Abstract

Hydrogen produced via water electrolysis powered by renewable electricity or green H_2 offers new decarbonization pathways. Proton exchange membrane water electrolysis (PEMWE) is a promising technology although current density, temperature and H_2 pressure of the PEMWE will have to be increased substantially to curtail the cost of green H_2. Here, we report a porous transport layer for PEMWE that enables operation up to 6 A cm^{-2}, 90 °C and 90 bar H_2 output pressure. It consists of a Ti porous sintered layer on a low-cost Ti mesh (PSL/mesh-PTL) by diffusion bonding. This novel approach does not require a flow field in the bipolar plate. When using the mesh-PTL without PSL, the cell potential increases significantly due to mass transport losses reaching ca 2.5 V at 2 A cm^{-2} and 90 ºC. On the other hand, the PEMWE with the PSL/mesh-PTL has same cell potential but at 6 A cm^{-2}, thus increasing substantially the operation range of the electrolyzer. Extensive physical characterization and pore network simulation demonstrate that the PSL/mesh-PTL leads to efficient gas/water management in the PEMWE. Lastly, the PSL/mesh-PTL was validated in an industrial size PEMWE in container operating at 90 bar H_2 output pressure.

1. Introduction

In recent years, carbon dioxide (CO_2) emissions have been increasing worldwide by more than 60 % from 1990 to 2019. [1] In April 2020, the "Mission 2020" was launched to strengthen the efforts and implementation of CO_2 reduction approaches in the key sectors [2], because even if CO_2 emissions remain constant in 2020, the goals of the Paris Agreement of 2015 can no longer be achieved. [3] Currently, about 48 % of today's hydrogen demand is produced from steam methane reformation, 30 % from crude oil cracking and 18 % from coal gasification, 3 % as chlor-alkali byproduct while only 1% is produced by water electrolysis. [4] If electricity from renewable energies is used for hydrogen production by electrolysis, this is also referred to as green hydrogen. [5,6] Recently, the European Union stressed the need for green H_2 to achieve carbon neutrality by 2050 [7] and plans to install 2 x 40 GW electrolyzer capacity by 2030. [8] In Europe, the overall investments in renewable hydrogen is to be increased to € 180-470 billion by 2050. [7] This unprecedented integration of large-scale electrolysis for the production of green H_2 can lead to a significant reduction in CO_2 emissions.

Two electrolysis technologies are particularly suitable for the implementation of green hydrogen production on the aforementioned scale. These include the already well matured, widely used alkaline water electrolysis (AWE) and the polymer electrolyte membrane water electrolysis (PEMWE). [9] The main difference between the two technologies is the electrolyte. While AWE uses an alkaline solution as electrolyte, PEMWE uses a solid membrane. This difference is directly coupled with advantages and disadvantages of the respective technology. Although AWE is a mature technology, it has the disadvantage that can only operate at low current densities and operating pressure. Most commercial AWE can operate up to 0.5 A cm^{-2} [10] while PEMWE has a nominal load of a about 2 A cm^{-2}. [11] However, the cost of PEMWE systems is lagging behind AWE, which is 33 % higher (900 € kW^{-1}). [12]

The widespread installation of PEMWE around the world for generating green H_2 has been increasing rapidly. For example, Hydrogenics installed an operational 1 MW PEMWE in

2016. [13] Already in 2018, Shell has started the installation of a 10 MW PEMWE from ITM Power in its refinery as part of the EU project REFHYNE, [14] which covers only up to 1% of the hydrogen consumption of the plant. Within the project "Westküste 100" the small refinery Heide, located near Hamburg, started the integration of a 30 MW electrolysis plant in the beginning of 2020, which will produce green hydrogen by using surplus offshore wind power and will be one of the first large scale demonstration plants of the energy transition or "Energiewende" in Germany. [15] BP, Nouryon and the Port Authority of Rotterdam are also working on a feasibility study for the installation of a 250 MW electrolysis plant to produce 45 kt H_2 per year. Nouryon, Orsted, ITM Power and their partners are also investigating the implementation and installation of a 1 GW electrolysis plant. [16,17] These extraordinary efforts contribute fundamentally to making green hydrogen competitive and thus potentially reducing CO_2 emissions significantly. Nevertheless, the IEA estimates that the cost of green H_2 should be 3.5-5 €/kg compared to 1.5 €/kg for grey hydrogen in order to be competitive. [18]

Basically, two approaches can be considered for cost reduction of PEMWE. On the one hand, costs can be reduced by replacing expensive stack materials such as Pt, Ir or Ti. However, this approach will compromise the performance or durability. Another and more realistic approach would be to operate the electrolyzer at conditions that will allow achieving high H_2 production rates. Thus, the highest demands of H_2 production from renewable energies for refuelling vehicles, grid stabilisation and reserve energy market as well as various industrial applications can be met. The following operation aspects are fundamental for performance enhancement:

i) High H_2 production rates by increasing the current density to reduce stack investment cost as well as stack volume
ii) High operating temperature to enhance cell efficiency
iii) High H_2 output pressure to avoid mechanical compression thus reducing costs and increasing efficiency on system level

Current standard operation range for commercial PEMWE is about 60 to 80 °C, 30 bar and a nominal current density of 2 A cm^{-2}. [11,19] Optimized PEMWE cell components have already been developed for these operating parameters. A scheme of a state-of-art (SoA) PEMWE single cell is shown in Figure 1 a). Core components are the membrane electrode assembly (MEA), porous transport layers (PTL) and the bipolar plates (BPP). The MEA consists of a proton exchange membrane (PEM) on which the anodic and cathodic catalyst layers are applied. The electrode catalysts consist of iridium or ruthenium oxides (IrO_x-RuO_x) on the anode side and platinum nanoparticles on carbon nanostructures (Pt/C) on the cathode side. The PTL on the anode, which is made of Ti, is an important key component, which needs to ensure effective media transport, specifically water transport from the flow field of the BBP to the electrodes and gas removal. It is well known that gas/water management strongly influences cell performance [20-22] and mass transport losses must be kept low. Therefore, this phenomenon becomes more relevant with increasing the applied electrical current, as the production rates of the gases increase. Anode PTLs that are commercially available vary from sintered powder structures, felts and meshes, but there are also new developments like tuneable PTLs with controlled parameters like porosity [23,24] and pore structure with size gradients [25,26]. Carbon paper is commonly used for the cathode PTL in PEMWE. [27]

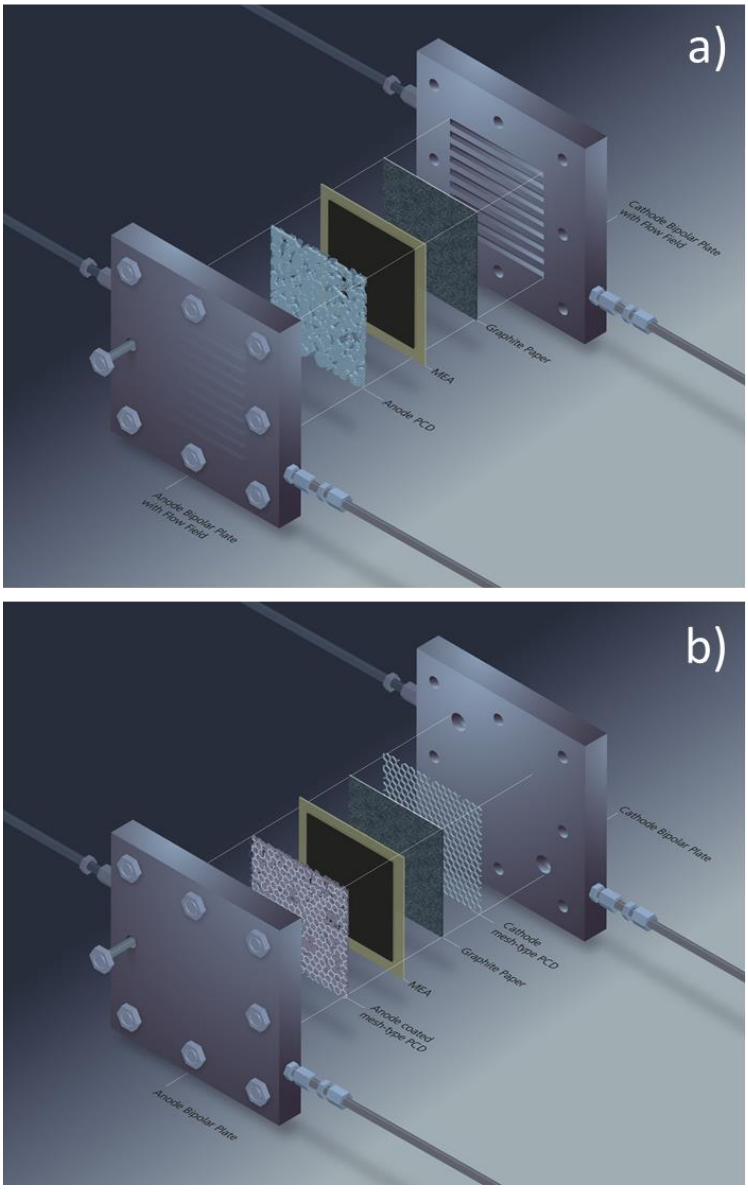

Figure 1. Schemes of PEMWE cell configurations: a) State-of-art (SoA) cell with Ti porous PTL which still requires a flow field in the BPP and b) cell with Ti PSL/mesh-PTL and BPP without flow field.

However, sophisticated PTLs for the anode need to be redesigned to minimize high overpotentials due to mass transport losses which reduce the cell efficiency. In this study we developed a novel PTL produced by diffusion bonding of a Ti porous sintered layer (PSL) on a Ti expanded metal sheet or mesh, allowing to dispense with the flow field in the BPP. The PTL was tested in a PEMWE under extreme conditions of current density,

temperature and pressure, that is up to 6 A cm^{-2}, 90 ºC and 90 bar. The PTL ensures efficient gas/water management at the high current densities. Finally, the functionality of the PTL at 90 bar H_2 output pressure was successfully validated in an industrial size PEMWE in container with a stack based on the hydraulic cell compression concept. [28-30]

2. Discussion of results

Morphology of the coatings

Photos of the PSL/mesh-PTL produced by diffusion bonding are presented in Figure S1 a) and b), which correspond to the side in contact with the BPP and MEA, respectively. The difference between the two surfaces is clearly visible in Figure 2: the hills and valleys of the expanded mesh in Figure 2 a) and b) that play a similar function as the flow field in the BPP and the dense surface of the PSL in cross-sectional images of Figure 2 c) and d) which contacts uniformly the catalyst layer. The morphology and the microstructural properties of the PSL/mesh-PTL were investigated by SEM.

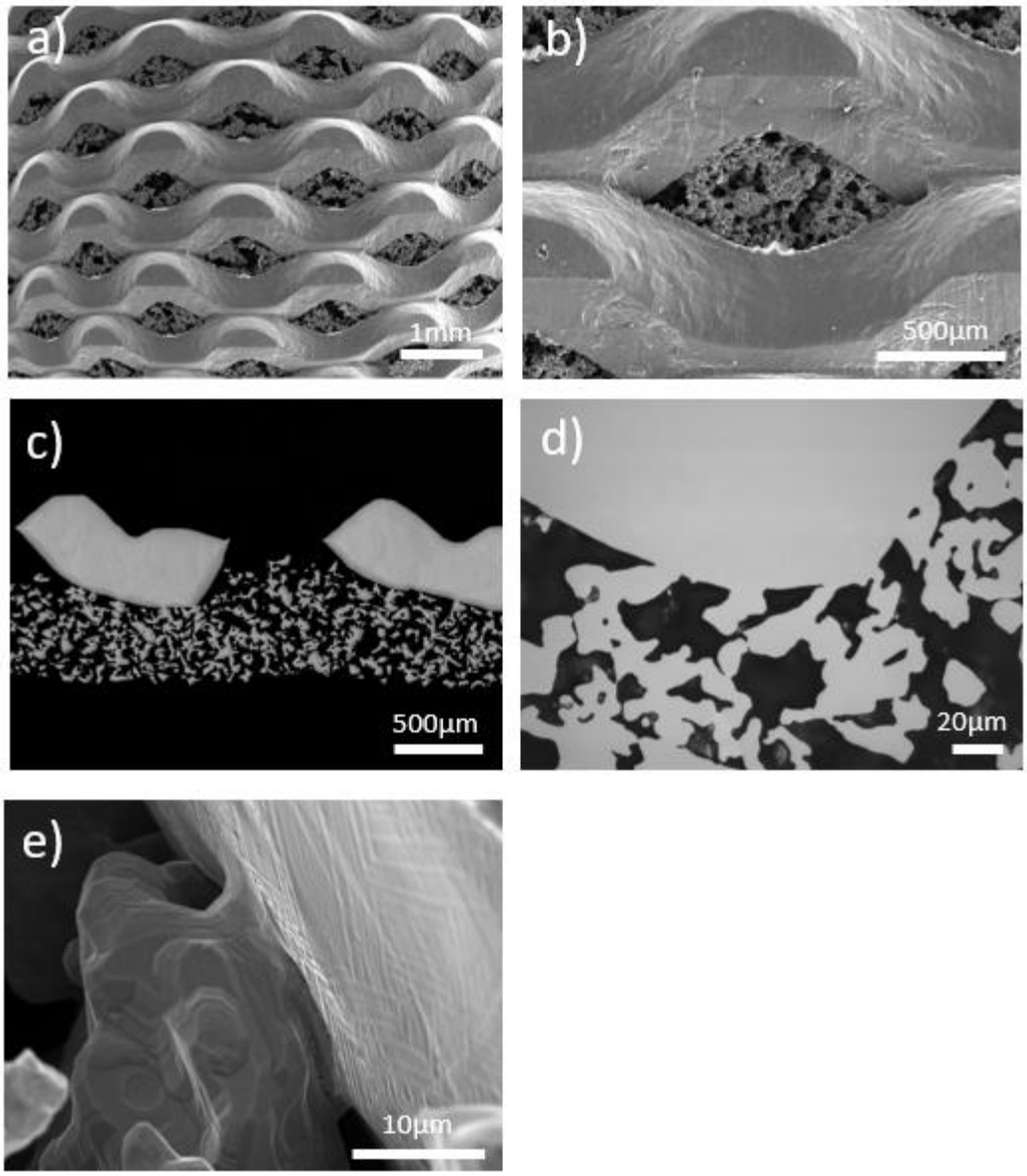

Figure 2. Images of PSL/mesh-PTL a) substrate side with low magnification, b) substrate side with high magnification as well as cross-sectional images of c) PSL/mesh-PTL with low magnification, d) PSL/mesh-PTL with high magnification and e) high magnification image of the interface of the mesh substrate and the macro-porous structure coating of PSL/mesh-PTL.

A homogeneous porous structure of the coated powder can be observed, which is diffusion bonded to the expanded mesh substrate. This detail is shown by a high-magnification image in Figure 2 e). While the PSL structure contacts the electrode, the mesh substrate is

correspondingly oriented towards the BPP distributing the applied current and managing gas/water transport. The fine porous structure closes completely the holes of the substrate mesh, avoiding that the MEA is pressed into the valleys of the expanded mesh during cell compression and is therefore protected from mechanical stress. [31] Cross-sectional images of the MEAs with and PSL/mesh-PTL are shown in Figure S2. Moreover, closing the holes of the mesh-PTL with the PSL is also advantageous as it increases the catalyst utilization. [32,33] Figure S3 presents PSL/mesh-PTL under polarized light. The polarized light provides particularly good contrast and visualization of the structure and grains of the Ti particles. Due to the heat treatment a classical α, β structure forms the composition of the PSL which can be observed under the polarized light. A uniform structure is the basis for a high stability of the sample under the corrosive conditions in the PEMWE, which Ti is known to withstand. [11]

Pore properties and ICR

The pore properties of PSL/mesh-PTL found by the bubble point, pore size distribution and permeability tests described in section 2.2.2 are presented in Table 1 summarizing sample thickness, pore size, density, porosity, bubble point and permeability. Real porous structures usually have more than just a certain pore size as in a supposedly ideal porous structure, which is why values are given for small pores (SP), mean flow pore (MFP) and large pores (LP). The pore size variation within the porous layer of the PSL/mesh-PTL ranges from 18 to 70 µm for the SP and LP, respectively, and a porosity of about 40 to 50 % can be determined.

Table 1. Pore properties from filter specific tests for PSL/mesh-PTL measured at the PSL.

Property	**PSL/mesh-PTL**
Thickness / mm	0.7 ± 0.1
Pore size / µm (calculated from Bubble Point)	52,3
Density / %	50-60
Porosity / %	40-50

SP* /µm	18
MFP* / µm	36
LP* / µm	70
Bubble Point / mbar (isopropanol)	18
Flow / $m^3\ h^{-1}\ m^{-2}$ (air, 1 mbar)	365
Permeability α / 10-12 m^2 β / m	 13,5 8,5

*measured at PSL

In addition to optimal pore properties, the electrical contacting of the samples within a cell plays an important role in achieving high performance. This can be evaluated by determining the ICR and was measured comparatively for PSL/mesh-PTL as well as for mesh-PTL. For the measurement, a setup was chosen that comes as close as possible to the conditions for the PTL in an electrolysis cell. Due to its high in-plane electrical conductivity, the carbon paper acts as a substitute for the precious metal-based electrode with which the PTL is contacted in the cell. Considering the ICR at a compaction force of 150 N cm^{-2}, which is typically used in commercial electrolyzer stacks [34], the PSL reduces the contact resistance by 43 % to about 58 mΩ cm^2 compared to the uncoated mesh. The results are presented in Figure 3.

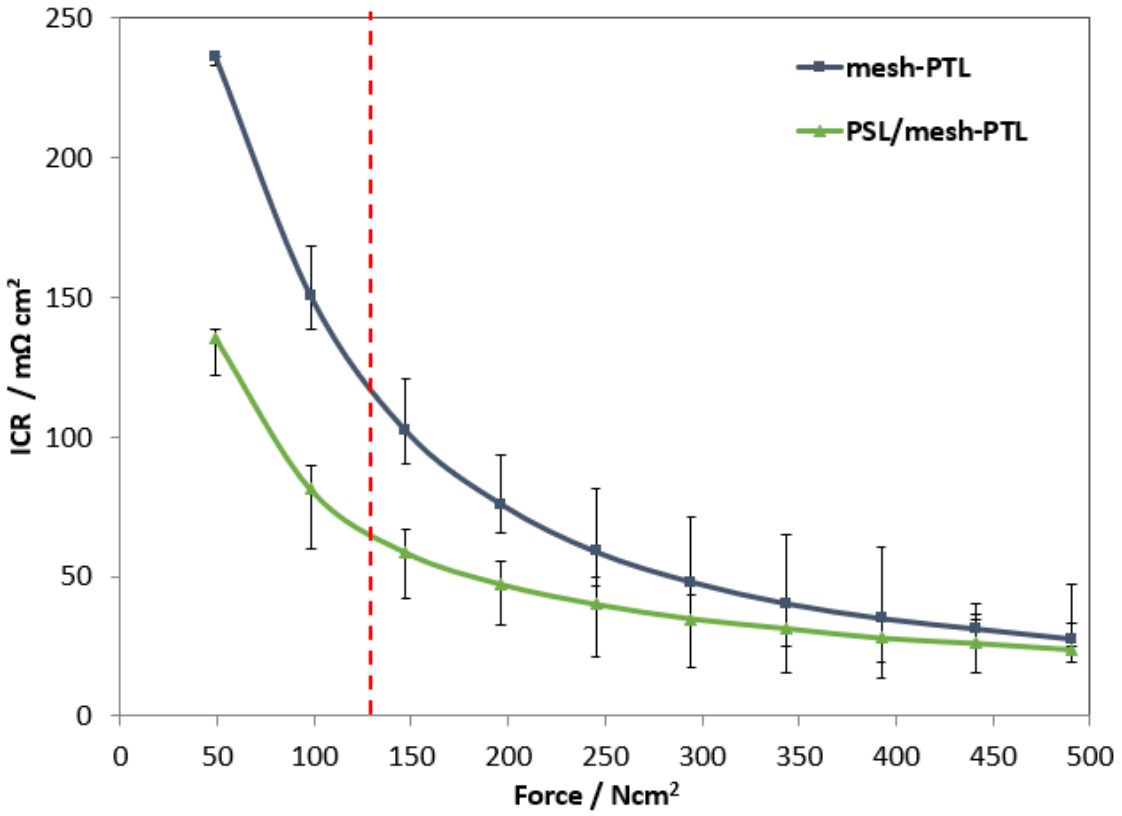

Figure 3. Interfacial contact resistance (ICR) with respect to compaction force of mesh-PTL and PSL/mesh-PTL. The slashed line indicates the typical compaction force of a commercial PEMWE stack.

Electrochemical performance and simulation

Figure 4 a) presents the E_{Cell}/j-characteristics of the PEMWEs using mesh-PTL and PSL/mesh-PTL up to 6 A cm^{-2}. For a PEMWE operated under extreme conditions, a current density of 4 A cm^{-2} can be considered as nominal load while 6 A cm^{-2} would correspond to overload. The cell with mesh-PTL is operable to a current density of only up to 4 A cm^{-2} already reaching an E_{Cell} of 2.89 V while not exceeding 3.0 V. Operation at this high potential is economically not attractive and oxides are formed on the surfaces of Ti components leading to higher ohmic resistance. Furthermore, a deviation between ascending and descending curve occurs which can be evaluated as a first indicator for mass transport losses according to earlier publications. [26] The upward bend of the curve corresponds to a limitation due to inefficient gas/water management. Expanded Ti meshes

as tested comparatively in this study have a clear price advantage over other expensive PTLs such as Ti felts but as demonstrated in Figure 4 a) they are far less efficient. In contrast, the cell with the PSL/mesh-PTL achieves a cell voltage of 2.54 V at 6 A cm^{-2} (overload) showing a polarization curve with a totally linear slope, and ca. 2.2 V at 4 A cm^{-2}. For comparison PEMWE commercial electrolyzers, such as those from Hydrogenics [35], Siemens [36] and Proton Onsite [37] achieve about 2.2 V at 2 A cm^{-2} while the PEMWE with the PSL/mesh-PTL allows operation at twice the current density at the same cell potential. However, currently these PEMWE operate in the temperature range of 60-80 ºC. The PSL/mesh-PTL combines low-cost Ti expanded mesh with a porous layer that allows reducing the cell overpotential by 693 mV at 4 A cm^{-2} compared to the mesh-PTL. Thus, an efficiency increase of 24 % can be achieved which has a significant impact on the operational cost of the electrolyzer.

Further, a deep explanation of the observed phenomena is given by electrochemical impedance spectroscopy (EIS). The Nyquist plots of the PEMWE with mesh-PTL and PSL/mesh-PTL at 0.25, 1 and 4 A cm^{-2} are given in Figure 4 b), c) and d), respectively. In earlier work, an equivalent circuit was introduced as a basis for the analysis of Nyquist spectra [26], which was further adapted and is described in the Figure S4. The ohmic resistance can be determined from the intersection of the first semicircle in the high-frequency range with the x-axis. Literature references assign the high-frequency arc to the hydrogen evolution reaction (HER), [38] charge transfer resistance coupled with double layer effects [35] or the first charge transfer of the 4-electron process of the oxygen evolution reaction (OER). The OER in the electrochemical splitting of water into O_2 is a 4-electron process (independent of the reaction mechanism and the catalyst used, i.e. Pt or IrO_2). The Krasil'shchikov mechanism formulated in C. Rozain et al. is only for 1/2 O_2, thus requiring only two electrons.[39] However, to generate O_2 it will require 4 electrons. The medium and low frequency semicircle can be attributed to the charge transfer of the OER rate determination step and the mass transport losses. [40]

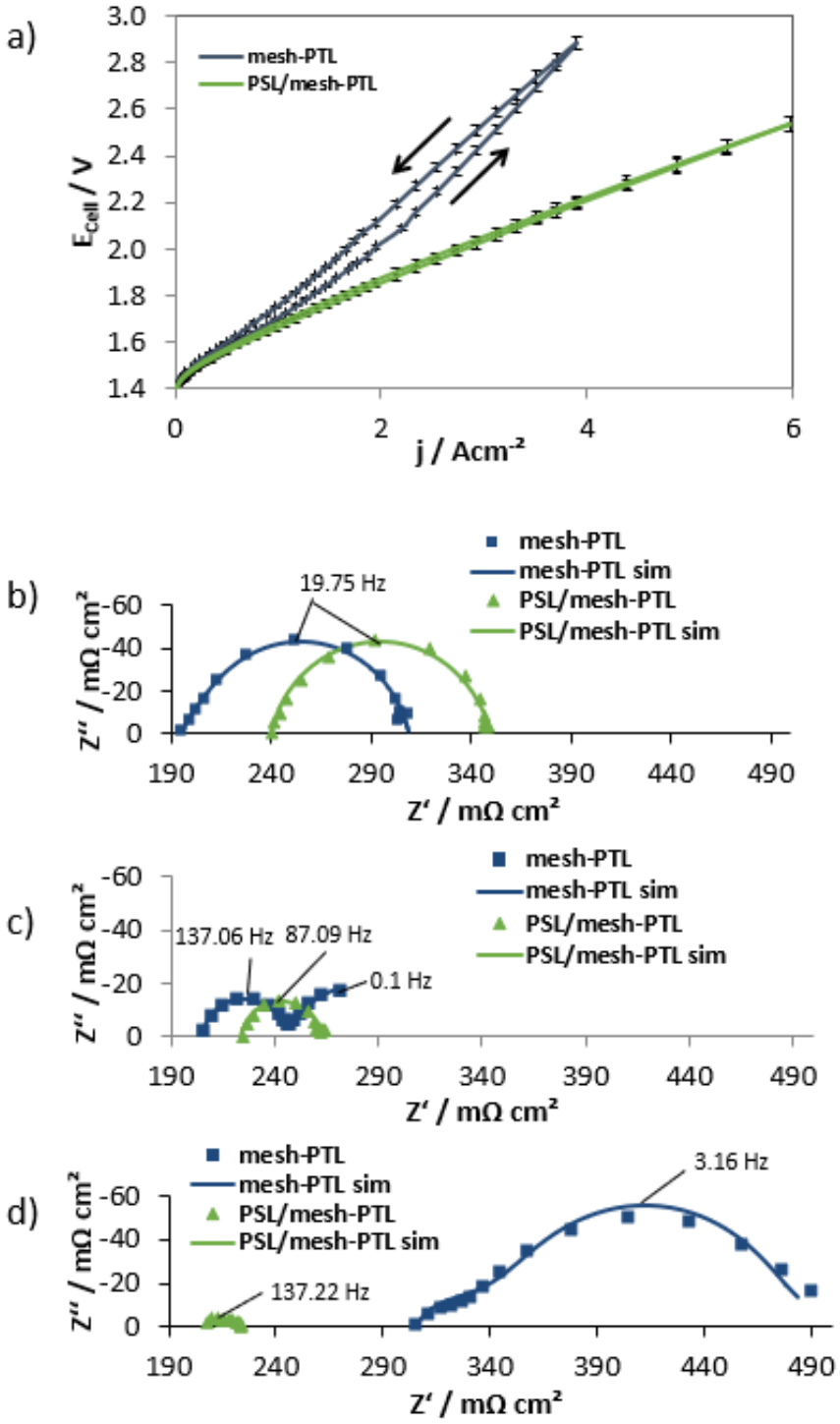

Figure 4. a) Polarization curves of PEMWE cells with mesh-PTL and PSL/mesh-PTL up to 6 A cm^{-2}. Nyquist plots at b) 0.25, c) 1 and d) 4 A cm^{-2} from 100 mHz to 50kHz. All measurements were carried out at 90 °C and ambient pressure.

At 0.25 A cm^{-2} for both samples one semicircle occurs with a peak at a frequency of 19.75 Hz and are thus mainly caused by charge transfer resistances with respect to OER. The difference between the mesh-PTL and PSL/mesh-PTL can be seen in the intersections with the real part axis, which results from the different ohmic resistance of the PTLs. The EIS at 0.25 A cm^{-2} reveals an ohmic resistance of 190 and 239 mΩ cm^2 for mesh-PTL and PSL/mesh-PTL. When increasing current density to 1 A cm^{-2} the semi-circles start to change in their behaviour. The ohmic resistance changes for both cells and the values approach each other. For mesh-PTL the resistance increases by 9 mΩ cm^2, while PSL/mesh-PTL decreases by 16 mΩ cm^2. For the cell with the mesh-PTL, the semicircle, which is associated to the OER kinetics, is insignificantly larger in size than for PSL/mesh-PTL with a maximum at 137.06 Hz. Only for mesh-PTL a second arc with an apex at 0.1 Hz appears, indicating mass transport losses. This is in good agreement with the polarization curves of the cell with mesh-PTL in which the slope starts bending upwards at about 1 A cm^{-2} while for the cell with the PSL/mesh-PTL the slope keeps a linear behaviour.

While at low currents the slow kinetics of the OER results in performance loss, for the cell with mesh-PTL the mass transport loss (MTL) become the determining factor at high current densities. At 4 A cm^{-2}, the ohmic resistance of the cell with the mesh-PTL increases to 306 mΩ cm^2 and the second semicircle related to MTL with a peak at 3.16 Hz enlarges considerably. Conversely, the arc associated with the OER in the cell with the PSL/mesh-PTL decreases in size as expected and shifts gradually to the left with the applied current density. The latter effect can be due to heat generation at the interface between the PSL and the electrode. Most notably, the arc associated to the MTLs is almost not visible even at 6 A cm^{-2}.

In order to explain the phenomenon of oppositely developing ohmic resistances for mesh-PTL as well as PSL/mesh-PTL at 1 as well as 4 A cm^{-2}, simulation data are interpreted. From these, the resistance caused by the MTL can be determined and accounts for 96 mΩ cm^2 (see Figure S5 b)). The high resistance associated with the MTL is caused by the absence of small pores at the contact surface of the uncoated mesh, which means that gas

bubbles can only be discharged to a limited extent by capillary forces, as the pore gradient is too small. [41] The gas blocks the active centres until a certain bubble size is reached. In addition, Ito et al. show that the bubble size depends on the pore size of the PTLs. [42] The larger gas bubbles increase the gas coverage of the transport channels and obstruct the water supply. This accumulation of gas at the interface of PTL/catalyst layer (CL) can also explain the increase in ohmic resistance due to the formed gas cushion which reduces the electrical contact between the components.

For the PSL/mesh PTL the ohmic resistance is 203 mΩ cm² and a second semicircle can barely be seen. With a modal pore diameter of 44 µm and increased porosity, the PSL/mesh-PTL ensures improved mass transport at high current densities. By simulating the Nyquist plots the resistance related to MTL can be determined and corresponds to 5.07 mΩ cm² (see Figure S5 b)) and therefore MTL can be neglected. Since MTL has been practically eliminated for the PSL/mesh PTL, the gas/water management is optimized, particularly at high current densities. As a result, the electrical contact, which is directly coupled to the ohmic resistance of the cell, is maintained. Due to the optimal electron and mass transport for the PSL/mesh-PTL, the loss processes for high current densities are minimal compared to the mesh-PTL.

The improved mass transport properties of the PSL/mesh-PTL can be explained by pore network modelling. The drainage curve acquired with the PSL/mesh-PTL, Figure 5 a), exhibited similar trends as reported in the literature with other PTLs. [43] Due to the larger pore openings at the mesh interface, the required capillary pressure to remove gas was lower (7143.55 Pa required to achieve 86 % gas saturation). In fact, the permeability of liquid water with gas saturated pores (also known as the two-phase permeability [44,45,52]) in the PSL/mesh-PTL was orders of magnitude higher than the predicted permeabilities of the liquid water in PTLs in previous work, [44,45] which implies that reactant delivery was more effective with the PSL/mesh-PTL. With both phases present, the permeability of liquid water and the permeability of gas have significant impacts on electrolyzer performance. The permeability of liquid water determines how effectively liquid water reactant reaches the reaction sites, and the permeability of gas determines how effectively

product gas is removed from the reaction sites. We previously reported that the flow of liquid water exerts a shear stress (proportional to its kinetic energy) on the counter-flowing gas traveling through the PTL. Increasing the permeability of the gas phase facilitates more gas removal in the PTL of an operating electrolyzer. [46] For conventional PEMWEs, permeability can be considered less energy-demanding flow mechanism as compared to two-phase flows in microscopic pores. However, the PEMWE used for this work have BPPs without flow field and water is not flowing. Therefore, there is practically no friction between the gas exiting and the water entering the electrolyzer and thus a two-phase mass transport mechanism was used for the calculation of permeabilities.

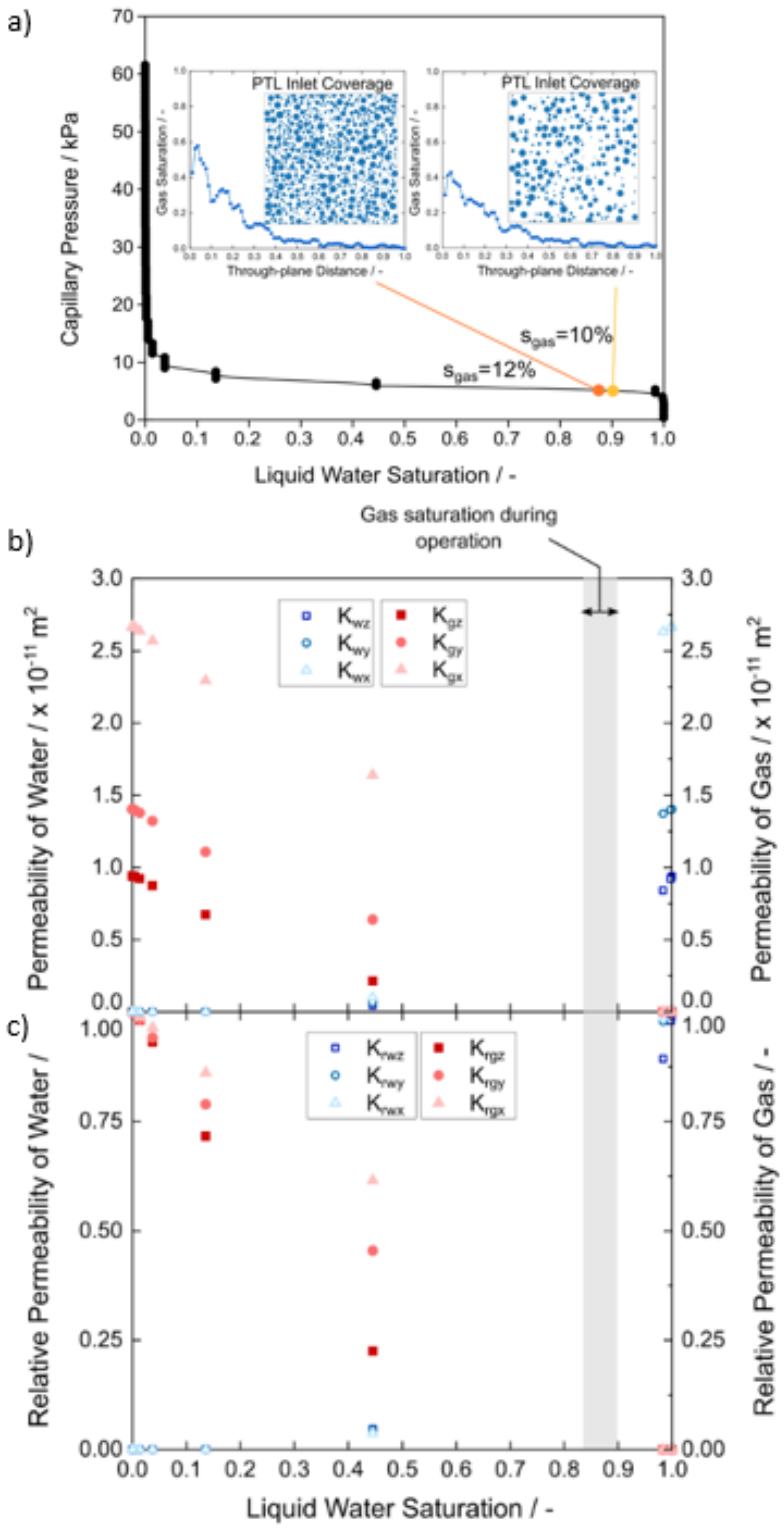

Figure 5. Pore network simulations that account for the mass transport mechanisms in the PSL/mesh-PTL. (a) drainage curve acquired for PSL/mesh-PTL. The subset figures indicate the gas surface coverage at the CL-PSL interface, simulating scenarios of high and

low current densities (750 and 250 inlet clusters) and their resultant gas saturation profiles. Although the number of inlet clusters increases significantly from 250 to 750 clusters (at the CL-PSL interface), the overall gas saturation only increases by 2% due to the effect of the porous structure of the PSL/mesh-PTL. (b) Permeability of liquid water and gas in the presence of both phase in the pore structure and (c) relative permeability (ratio of the permeability of liquid water with and without presence of gas saturated pores) of the PSL/mesh-PTL. The grey shaded region (gas saturation during operation) was obtained by performing invasion percolation with varying inlet coverage as shown in (a).

Based on invasion percolation simulations with various inlet conditions, the gas saturation in the PTL remained significantly low (12%) even at the high surface coverage of gases at interface with the catalyst layer, 750 inlet clusters, subset of Figure 5 a). The low gas saturation of the PSL/mesh-PTL is due to the porosity gradient resulting from a bilayer structure of the PSL and mesh-PTL. Previous modelling results in literature [42] reported significant reduction in gas saturation (up to 70% reduction of gas saturation) when lower porosity was positioned next to the catalyst layer. The low gas saturation in the PSL/mesh-PTL suggested that even at high current density operation, the generated gases would be effectively removed via larger pores in the PTL. Therefore, the PSL/mesh-PTL exhibited high permeability of both liquid water and gas as shown in the grey regions of Figure 5 b) and c), providing effective two-phase transport for higher current density operations.

Validation in high H_2 pressure system

Due to safety reasons, the evaluation of the PSL/mesh-PTL in a PEMWE that produces high H_2 pressure requires an industrial system in a container such as the one shown in Figure 6 a). For these tests, only the PSL/mesh-PTL was tested in the stack as the cells with the mesh-PTL cannot keep the E_{Cell} low at high current densities. In Figure 6 b) an exemplary E_{Cell}/j-characteristic of this test cell is recorded at ca. 52 °C, 95 bar oxygen pressure and up to 6 A cm^{-2} resulting in a voltage at peak current density of 2.98 V. Currently, it is not possible to reach 90 ºC. In a conventional stack design, the temperature increases sharply along with current density causing the bending of the polarization curve.

[35] However, a stack based on hydraulic compression technology is designed to dissipate heat in a very efficient way through the hydraulic media ensuring a homogeneous temperature over the cell area. In this regard, to reach 90 ºC the balance of plant (BoP) of the PEMWE requires a retrofitting system, which is currently under development. Therefore, at present it is not possible to evaluate the PSL/mesh-PTL under the three extreme conditions of operation all at the same time due to the PEMWE system limitations. That is, the PEMWE can operate either under 6 A cm^{-2}, 90 ºC, and 1 bar or 6 A cm^{-2}, 52 ºC, and up to 90 bar. In any case it is clearly proven that the PSL/mesh-PTL can withstand the three extreme conditions of operation. By using a simple numerical model based on the Nernst equation one can simulate the polarization curve at 1 and 90 bar which are shown as dashed lines in Figure 6 b) at 52 and 90 °C. The calculated E_{Cell} of the stack at 6 A cm^{-2}, 90 ºC and 90 bar is comparable to the one achieved with single cell measurements. The details for the calculation of the cell voltage can be taken from the SI.

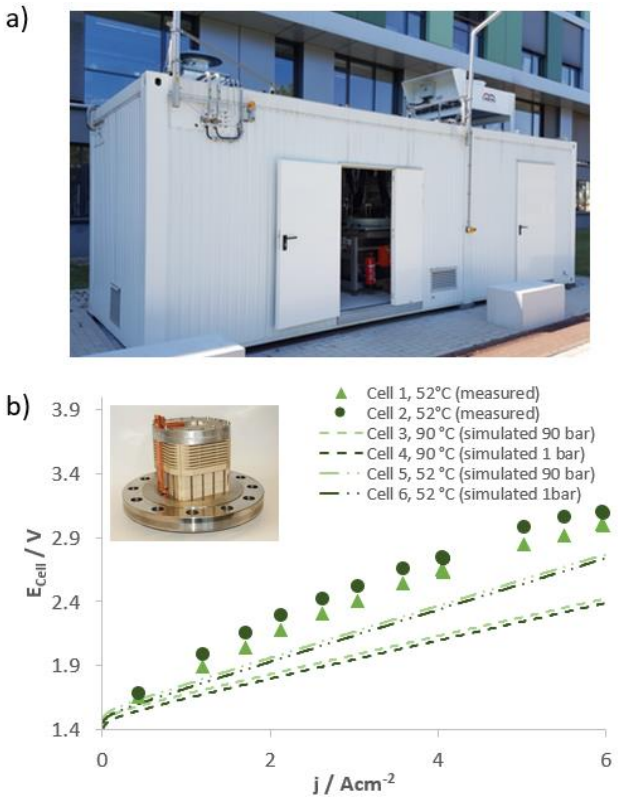

Figure 6. a) Photo of the PEMWE system for a maximum production of 5 $Nm^3\ h^{-1}$ integrating the stack showed b) Polarization curve with PSL/mesh-PTL at pressure of 1 and 90 bar at 52 °C and 90 °C up to 6 A cm^{-2}. The dashed lines represent the simulated polarization curve of PSL/mesh-PTL at 1 and 90 bar as well as 90 °C up to 6 A cm^{-2}. A photograph of the utilized stack based on hydraulic cell compression is shown in the inset. Following the polarization curve from Figure 6 b), a durability test was carried out for 600 hours. The stack was operated at 65 °C and constant 2 A cm^{-2}. The results show a negligible degradation rate of 4.43 µV h^{-1} and can be seen in Figure S7.

Translating the results presented in this work to the current market needs, the cost of green hydrogen can be significantly reduced. The integration of intermittent renewable energy into the power grid, including the provision of balancing power, raises new requirements in terms of efficiency, flexibility, partial load and stand-by operation, PEMWE capacity (GW scale plants) and investment cost (CAPEX) depending on the specific application/operation strategies. By operating the PEMWE at high current density and maintaining SoA cell efficiency, an increased H_2 production rate can be achieved, which reduces costs further. Higher specific H_2 production rates reduce the stack volume, lower the system costs, decreases the footprint of the electrolyzer and ultimately bring closer the widespread utilisation of green H_2 in the industry and mobile sectors.

One remaining question is about long-term stability of the PSL/mesh-PTL. Certainly, PEMWE cell components may degrade faster under operation at extreme conditions. However, the PSL/mesh-PTL is made of Ti and at nominal operation, which we defined now at 4 A cm^{-2}, the E_{Cell} is still kept low, thus no excessive formation of TiO_x is expected. Moreover, operating at 90 ºC instead of 65º C will not increase significantly the rate of Ti oxidation. Lastly, thanks to hydraulic cell compression technology, the mechanical stress on the PSL/mesh-PTL is lower than what it would be in the traditional PEMWE designs. Operation at highly stressing conditions will most likely have an impact on the PEM and ionomer of the MEA as well as on the BoP components. Therefore, more R&D is needed on these topics to bring to the market a PEMWE that can operate at extreme conditions of current, density, and pressure.

3. Conclusion

We have developed a novel PTL for PEMWE by sintering a macro-porous structure of Ti on an expanded Ti mesh, PSL/mesh-PTL, thus producing a fully functional cell component with enhanced properties. The PSL has uniform pore size distribution and porosity and is fully bonded via diffusion to the mesh-PTL, which eliminates any interfaces that cause ohmic losses. From the PEMWE tests, the PSL/mesh-PTL allows achieving up to 6 A cm^{-2}, 90 °C and 90 bar H_2 output operation. The PEMWE with the PSL/mesh-PTL reached 31 % higher efficiency than the mesh-PTL at a nominal load of 4 A cm^{-2}. Pore network modelling showed that the large increase in performance is attributed to the high permeability for both liquid and gas for the PSL/mesh-PTL, providing effective two-phase transport at high current densities. The PSL/mesh-PTL design addresses all tasks in the cell regarding water distribution and gas transport, thereby eliminating the need for a bipolar plate with a complex flow field. Operating PEMWE at high current density, temperature and pressure makes it more economically attractive. In the near future, these challenging operating conditions can be established as the new SoA in electrolysis for the large-scale integration of renewable energies, thus reductions in CO_2 emissions can continue at more aggressive pace. The PSL/mesh-PTL presented in this work will be now a commercial product and possible interested laboratories can order it from GKN Sinter Metals.

4. Experimental

PSL on Ti-mesh by diffusion bonding

Fine Ti powder and a supporting expanded mesh were used to produce porous, asymmetrically structured current distributors. Both deployed raw materials are composed of grade 1 titanium. These expanded metal sheets are produced by cutting slits into a plate and stretching this plate afterwards. This process creates a specific pattern with open gaps resulting in an open porosity of 55 %. Subsequently, Ti powder was deposited on the expanded mesh to produce the PSL.

The deposition technique has been optimized so that a homogeneous layer on the structural supporting material is generated. Next step is diffusion bonding via a sintering process to generate a firmly bonded asymmetric compound structure. The heat treatment is performed under a vacuum of 2 x 10^{-5} mbar to prevent oxide formation. Typically, the sinter temperature is 70 % of the absolute melting temperature. The optimal sinter temperature varies also within the particle size distribution of the metal powder: the finer the powder the higher the diffusion activity. The batch furnace used for heat treatment is build up with metal heating elements and metal shielding without any graphite elements to prevent carbide formation. The produced PTL is labelled as PSL/mesh-PTL. In order to obtain a better understanding of the PSL properties, a similarly produced porous film (without expanded metal sheet) was prepared and examined so that the specific pore properties could be determined without any loss in accuracy due to the larger pores of the mesh compared to those of the PSL which would affect the measurements.

Physical characterization

4.1.1 Polarized light microscopy

A microscope system for materials research was used for analyzing the coating quality as well as the morphology of the produced coated samples. Cross-section images were recorded with a Zeiss AXIO Imager.A2m using a Jenoptik ProgRes Speed XT core 5 camera. Furthermore, polarized light was used to determine the structure and grains of the material by interference, depending on the sample thickness, birefringence and the resulting light path difference.

4.1.2 Filter specific tests and X-ray computer tomography (CT)

Filter specific tests like bubble point, pore size distribution, permeability as well as µCT measurements were carried out to characterize the morphology and sample properties.

Bubble point measurements were performed according to ISO 4003: “Permeable sintered metal materials; Determination of bubble test pore size” for filter, bearings and porous electrodes, which have an inner connected pore structure. The measured pressure value gives information of the (theoretical) apparent maximum pore size which could be determined by the formula (Eq. 1):

$$d = \frac{4 * \delta * cos\varphi}{\Delta p} \qquad \text{Eq. 1}$$

Here, d, δ, φ, and Δp are the apparent pore size, surface tension, contact angle and differential pressure, respectively. This pore size merely relates to idealized cylindrical pore structures, and a determination was performed by infiltrating a test specimen with an appropriate liquid with known surface tension via sample immersion. An increasing gas pressure is charged to one side of the specimen until one first bubble could be detected. The minimum gas pressure that is required to force liquid out of the capillary is called the bubble point pressure.

According to ASTM E 1294 pore size distribution measurement was conducted. This standard test enables calculation of the pore size distribution according to largest pore (LP), mean flow pore size (MFP) and smallest pore (SP) within a filter medium and is based on the bubble point test. Therefore, an automated liquid PMI porometer was used. The specimen to be examined was infiltrated with Topor (16.0 mN m^{-1}, Topas GmbH). Gradually gas pressure was increased to charge the porous specimen until the test liquid was removed and all pores were free from test liquid. During the test the flowrate was accurately recorded by the porometer. Afterwards a second test run without test liquid was executed. From the measured gas pressure and flow rates the pore diameters, the pore size distribution and the gas permeability could be calculated.

The third physical characterization was the determination of permeability following ISO 4022 “Permeable sintered metal materials - determination of fluid permeability” giving information on how well a medium, gas or liquid, flows through a porous filter. For the

calculation of permeability, the applied pressure, the pressure-drop across the filter and the flowrate are needed. Usually air is used for flow rate measurement. The viscosity of the flowing medium is an important parameter for the flowrate as a function of pressure drop. The fluid permeability can be expressed in terms of viscous and inertia permeability coefficients as follows:

$$\Delta p = \frac{\dot{V} \cdot s}{A} \cdot \left[\frac{\eta}{\alpha} + \frac{\rho \cdot \dot{V}}{\beta \cdot A}\right] \qquad \text{Eq. 2}$$

α, β, s, $\dot{V}$, ρ, Δp, A, and η express here viscosity coefficient, inertia coefficient, filter thickness, flow rate, fluid density, pressure drop at the filter, filter area and dynamic viscosity.

X-ray CT analysis was performed with a multi-scale X-ray microtomograph (Skyscan1172, Bruker). The reconstructed sample volume was 1760.3 x 4239.6 x 3599.6 μm^3, achieving a resolution of 1.43812 µm. An acceleration potential of 80 kV was used.

Interfacial Contact Resistance (ICR)

The influence of the PSL on interfacial contact resistance of the PSL/mesh-PTL with respect to the compaction force was measured according to previously published methodology. [34] After all PTL samples were cleaned by immersing in deionized (DI) water and isopropanol baths while applying ultrasonication for 10 minutes for each step a final cleaning cycle was carried out with DI water for 5 minutes. The PTL samples were placed in an oven for 20 minutes at 60 °C for drying. To measure ICR the cleaned PTLs were placed in between a titanium plate (3.7025) and a TGP-H-90 and sandwiched by two gold-coated copper cylinders. A hydraulic press, in which this setup was placed, was used to apply a weight of 20 to 200 kg in steps of 20 kg. A potentiostat/galvanostat (Zahner Elektrik IM6) with a booster (Module PP240) was connected to the cylinders applying a constant current of 1.25 A cm^{-2}. The response voltage was monitored. Determination of the ICR between the carbon paper and the PSL was calculated by the following equation:

$$R_{C/Coating} = R_{measured} - R_{C/Au}, \quad \text{Eq. 3}$$

where $R_{C/Au}$ can be assigned to the ICR of the gold coated cylinder. An uncoated mesh-PTL made of Ti was also measured for comparison purposes.

PEMWE tests

The samples to be tested were investigated using cells having different cell sizes and ranging from laboratory to system scale. First electrochemical characterization was performed using a laboratory cell with an active area of 4 cm^2. On the anode side Ti-BPP grade 1 and PSL/mesh-PTL were used while on the cathode side an uncoated carbon paper (TGP-H-90) as well as multilayer stainless steel mesh-PTL (Haver & Boecker OHG) and stainless steel BPP with 1.4404 grade were used. An Ir-based anode, Pt-based cathode and chemically stabilized Nafion 115 membrane were used as MEA for all electrochemical tests. The catalyst loading is 2.5 mg cm^{-2} for iridium and 0.95 mg cm^{-2} for platinum. Based on the results from a torque study of the described cell arrangement and considering mechanical stress at high compaction force the cells were tensioned with 1 N m. Polarization curves up to 6 A cm^{-2} were recorded and electrochemical impedance spectroscopy (EIS) was performed at 0.25, 1 and 4 A cm^{-2} and an amplitude of 100, 200, and 500 mA, respectively, from 100 mHz to 50 kHz. Both electrochemical characterizations were performed according to JRC protocols. [47,48] A potentiostat/galvanostat (Zahner Elektrik IM6) with a booster (Module PP240) was used for these measurements, which were carried out at 90 °C and ambient pressure. For comparison reasons the mesh-PTL was measured.

For the tests at high H_2 output pressure, the PSL/mesh-PTL was evaluated in a 5 $Nm^3 h^{-1}$ PEMWE system in container using a stack design based on hydraulic cell compression. For the study described in this work, a stack was developed based on R&D results which were described elsewhere. It has been shown that for earlier PEMWE prototypes homogeneous cell compression is achieved over the active cell area due to a hydraulic cell

clamping. [49] The principles and benefits of hydraulic cell compression were adapted to develop an advanced PEMWE prototypic stack for high operation temperatures, high current density and high operation pressure up to 90 °C, 6 A cm^{-2} and 100 bar.

Single electrolyzer cells are also completely surrounded by a hydraulic medium, while the pole plates (PP) are utilized as part of the flexible pockets, in which the active material is integrated. [50] By increasing the pressure level of the hydraulic medium, compression forces are applied to the PEMWE cell's PP through their intrinsic flexibility. As a result, the pressure level is equal in each point of the active cell area and, therefore, cell compression is as well homogeneous as adjustable to increasing hydrogen production pressures. Furthermore, a circulation of the hydraulic medium is established with an integrated heat exchanger for waste heat removal facilitating even temperature conditions for investigated cells. Controlling temperature and pressure of the hydraulic medium results in reproducible test conditions, which can be precisely adjusted.

The utilized PEMWE test stack comprised two cells with PSL/mesh-PTLs. Similar MEAs as in the single cell measurements were used. The active cell area for the cells investigated in this study was 210 cm^2. Polyetheretherketone (PEEK) was chosen as frame material to integrate the active components, due to its inertness, especially against the process water as well as evolving hydrogen and oxygen. For the analysis reported in this study, it has been integrated into a specially developed 5 N $m^3 h^{-1}$ containerized test system shown in Figure 6 a) for high-pressure operation.

Polarization curves were recorded up to 6 A cm^{-2} at 52 °C with oxygen and hydrogen output pressure of 95 and 90 bar, respectively. Later, it will be justified why the stack could only reach 52 ºC and not 90 ºC. In contrast to conventional stack designs with mechanical compression, the innovative design [28-30] allows homogeneous temperature distribution and cell compression. Therefore, hotspots due to inhomogeneous current density distribution or mechanical stress can be avoided enabling the ambitious operating parameters.

Numerical modelling

Two-phase transport properties of the PSL/mesh-PTL was simulated using pore network modelling via an open-source pore network model (OpenPNM). [51] For a more detailed description of the pore network modelling on PTLs for PEMWE, the readers are directed to the following studies. [44,45,52] For the pore network model implemented in this work, while the pores are represented as spheres connected by cylindrical throats, the total volume of the pore space itself was unaltered. The drainage of liquid water (wetting phase in a hydrophilic PTL) via the quasi-static invasion of oxygen gas (non-wetting phase) was used to simulate two-phase flow inside the anode compartment of the PEMWE. The nature of gas invasion into a water filled PTL is dominated by the entry capillary pressures of the throats. Specifically, during drainage, the gaseous phase preferentially invades pores connected to throats with the lowest capillary pressure. In this work, the capillary pressure of all pores and throats were calculated using the Young-Laplace equation:

$$P_C = \frac{-2\gamma \cos\theta}{r} \qquad \text{Eq. 4}$$

where P_C is the capillary pressure (Pa), γ is the surface tension ($N \cdot m^{-1}$), r is the radius of a pore throat (m), and θ is the contact angle (radians). The drainage curve of the PSL/mesh-PTL was obtained by incrementing capillary pressure until the PTL became fully void of liquid water from an initially fully wet condition.

The permeability was used as an indicator to predict mass transport in the PTL. The single-phase permeability (permeability of one phase in a porous structure) is solely the property of the porous structure. However, permeability values change in the presence of the second phase. Specifically, when the second phase occupies pore spaces, the permeability of the first phase is reduced. Herein, we refer to this permeability as the permeability of liquid water, which illustrates the effectiveness of the PTL to facilitate the delivery of reactants to the reaction sites in the presence of oxygen gas. Permeability of gas also illustrates the effectiveness of the PTL to facilitate the removal of the by-product gases from the reaction

sites in the presence of liquid water. To calculate the permeability of the PTL, the net flow into each pore was first determined by applying the conservation of mass to each pore:

$$q_i = \sum_{j=1}^{n} g_{h,ij}\left(P_j - P_i\right) = 0 \qquad \text{Eq. 5}$$

where *i* and *j* are the current and neighbouring pores, respectively. q_i is the net flow in pore *i* ($m^3 \cdot s^{-1}$), *P* is the pressure at each pore ($kg \cdot m^{-1} \cdot s^{-2}$), and $g_{h,ij}$ is the hydraulic conductivity for flow between each neighboring pore ($m^4 \cdot s \cdot kg^{-1}$), which was calculated with the Hagen-Poiseuille model [53]

$$g_h = \frac{\pi r^4}{8L\mu} \qquad \text{Eq.6}$$

where *r* is the radius of a pore or throat (m), *L* is a length of a pore or throat (m), and μ is the dynamic viscosity ($kg \cdot m^{-1} \cdot s^{-1}$). The net hydraulic conductivity was then calculated with linear resistor theory using values of hydraulic conductivities for half of pore *i*, the connecting throat, and half of pore *j*:

$$\frac{1}{g_{h,ij}} = \frac{1}{g_{h,pi}} + \frac{1}{g_{h,t}} + \frac{1}{g_{h,pj}} \qquad \text{Eq. 7}$$

The total flow, *Q* ($m^3 \cdot s^{-1}$), across the PTL was solved from a set of linear equations (Eq. 5) in conjunction with the prescribed pressure boundary conditions at the inlet and outlet of the PTL. Using Darcy's law the permeability of the PTL was calculated as follows:

$$\mathrm{Q} = \frac{KA}{\mu l}\left(P_{in} - P_{out}\right) \qquad \text{Eq. 8}$$

where *K* is the permeability (m^2), *A* is the cross-sectional area of the PTL (m^2), and *l* is the length of the PTL in the flow direction (m).

The invasion percolation simulation with varying inlet conditions was implemented to predict gas saturation in an operating PEM water electrolyzer. A number of gaseous droplets (with diameters randomly selected between 7.5 to 60 μm) were stochastically placed at the CL-PTL interface to mimic realistic operating conditions. A set of 250 inlet droplets was used to represent low current density operation, and 750 inlet droplets were used to represent high current density operation. Only the pores connected to the inlet droplets (or clusters connected to the inlet droplet) were considered for invasion at each step; therefore, gas filling occurred sequentially from the catalyst layer interface, and the invasion percolation simulation was considered completed when the pore at the outlet was invaded. It was assumed that after the point of breakthrough, subsequent gas removal takes place via these deterministically established gas pathways, as has been shown in previous studies. [54,55]

Acknowledgments

The research leading to these results has received funding from European Union's Horizon 2020 research and innovation program under grant agreement No 779478 (PRETZEL project) supported by FCH JU. The authors thank to Ina Plock, Jörg Bürkle and Henrike Schmies for performing SEM measurements, technical support and µCT measurements, respectively. The authors also acknowledge the support from A. Üstün in carrying out the PEMWE measurements as part of her master thesis. J. K. Lee is grateful for graduate scholarships awarded from the Natural Sciences and Engineering Research Council of Canada (NSERC) Alexander Graham Bell Canada Graduate Scholarships – Doctoral Program, Queen Elizabeth II/Edward Rygiel Graduate Scholarship in Science and Technology, Ontario Graduate Scholarship, and Glynn Williams Fellowships. Finally, the authors acknowledge Vincent Wilke for supporting the preparation of the revised version of the manuscript as the first author Svenja Stiber was in maternity leave during the revision process.

Additional information

Supplementary information is available for this paper.

Competing interests

The authors declare no competing interests.

References

[1] IEA, Global CO_2 emissions in 2019, IEA, Paris https://www.iea.org/articles/global-co2-emissions-in-2019, accessed: July, **2020**.

[2] Mission 2020, https://mission2020.global/, accessed: July, **2020**.

[3] Ch. Figueres, H. J. Schellnhuber, G. Whiteman, J. Rockström, A. Hobley, S. Rahmstorf, *Nature* **2017**, 546, 593-595.

[4] D. Bessarabov, P. Millet, *P. PEM Water Electrolysis (Volume 1)*, Hydrogen and Fuel Cells Primer Series, Academic Press **2018**.

[5] IRENA, Green Hydrogen Cost Reduction – Scaling up electrolysers to meet the 1.5 °C climate goal, International Renewable Energy Agency (IRENA), Abu Dhabi, https://irena.org/publications/2020/Dec/Green-hydrogen-cost-reduction, accessed: February, **2021**.

[6] Hydrogen Europe, Hydrogen Production, https://hydrogeneurope.eu/hydrogen-production-0, accessed: February, **2021**.

[7] European Commission, Communication from the commission to the European Parliament, the Council, the European Economic and Social Committee and the Committee of the Regions – A hydrogen strategy for a climate-neutral Europe, Brussels https://ec.europa.eu/energy/sites/ener/files/hydrogen_strategy.pdf, accessed: 07/2020.

[8] A. Van Wijk, J. Chatzimarkakis, Green Hydrogen for a European Green Deal – A 2x40 GW Initiative, Hydrogen Europe, https://hydrogeneurope.eu/sites/default/files/Hydrogen%20Europe_2x40%20GW%20Green%20H2%20Initative%20Paper.pdf, accessed: July, **2020**.

[9] D. Bessarabov, H. Wang, H. Li, N. Zhao, *PEM Electrolysis for Hydrogen Production: Principles and Applications*, CRC Press **2015**.

[10] S. A. Grigoriev, V. N. Fateev, D. G. Bessarabov, P. Millet, *Int. J. Hydrogen Energy* **2020**, 45 (49), 26036-26058.

[11] M. Carmo, D. L. Fritz, J. Mergel, D. Stolten, *Int. J. Hydrogen Energy* **2013**, 38, 4901–4934.

[12] FCH-JU, *Addendum to the Multi-Annual Work Plan 2014-2020*, Fuel Cells and Hydrogen 2 Joint Undertaking **2018**.

[13] Dena (Deutsche Energie-Agentur), WindGas Hamburg. https://www.powertogas.info/fr/projektkarte/windgas-hamburg/, accessed: 02/2020.

[14] REFHYNE, Clean Refinery Hydrogen for Future, https://refhyne.eu/, accessed: February, **2020**.

[15] WESTKÜSTE 100, https://www.westkueste100.de/en/, accessed: July, **2020**.

[16] ITM-Power, Gigastack Feasibility Study with Orsted, https://www.itm-power.com/item/58-project-to-demonstrate-delivery-of-bulk-low-cost-and-zero-carbon-hydrogen-through-gigawatt-scale-pem-electrolysis-manufactured-in-the-uk, accessed: July, **2020**.

[17] Van Delft, Y., Starting signal for design of gigawatt electrolysis plant, TNO, https://www.tno.nl/en/about-tno/news/2019/3/starting-signal-for-design-of-gigawatt-electrolysis-plant/, accessed: July, **2020**.

[18] IEA, The Future of Hydrogen – Seizing today's opportunities, IEA, Paris https://webstore.iea.org/download/direct/2803, accessed: July, **2020**.

[19] A. Buttler, H. Spliethoff, *Renew. Sustain. Energy Rev*. **2018**, **82**, 2440–2454.

[20] M. Suermann, K. Takanohashi, A. Lamibrac, T. J. Schmidt, F. Büchi, *J. Electrochem. Soc.* **2017**, 164 (9), F973-F980.

[21] K. Bromberger, G. Jagdishkumar, T. Lickert, A. Fallisch, T. Smolinka, *Int. J. Hydrogen Energy* **2018**, 43 (5), 2556–2569.

[22] T. Lickert, M. L. Kiermaier, K. Bromberger, G. Jagdishkumar, S. Metz, A. Fallisch, T. Smolinka, *Int. J. Hydrogen Energy* **2020**, 45 (11), 6047–6058.

[23] Z. Kang, J. Mo, G. Yang, S. T. Retterer, D. A. Cullen, T. J. Toops, J. B. Green Jr, M. M. Mench, F.-Y. Zhang, *Energy Environ. Sci.* **2017**, 10, 166–175.

[24] T. Schuler, R. De Bruycker, T. J. Schmidt, F. Büchi, *J. Electrochem. Soc.* **2019**, 166 (4), F270-F281.

[25] P. Lettenmeier, S. Kolb, F. Burggraf, A. S. Gago, K.A. Friedrich, *J. Power Sources* **2016**, 311, 153–158.

[26] P. Lettenmeier, S. Kolb, N. Sata, A. Fallisch, L. Zielke, S. Thiele, A. S. Gago, K. A. Friedrich, *Energy Environ. Sci.* **2017**, 10, 2521–2533.

[27] S. Park, J.-W. Lee, B. N. Popov, *Int. J. Hydrogen Energy* **2012**, 37 (7), 5850-5865.

[28] M. Brodmann, M. Greda, C. Mutascu, J. Roth, WO2011/069625A1, **2011**.

[29] M. Brodmann, M. Greda, C. Mutascu, J. Neumann, U. Rost, J. Roth, A. Wildometz, WO2014/040746A1, **2014**.

[30] M. Brodmann, C. L. Mutascu, P. Podleschny, U. W. Rost, J. Roth, C. Sagewka, F. J. Wirkert, WO2018/001543A1, **2018**.

[31] J. Mo, Z. Kang, G. Yang, S. T. Retterer, D. A. Cullen, T. J. Toops, J. B. Green Jr., F.-Y. Zhang, *Applied Energy* **2016**, 177, 817-822.

[32] Z. Kang, G. Yang, J. Mo, S. Yu, D. A. Cullen, S. T. Retterer, T. J. Toops, M. P. Brady, G. Bender, B. S. Pivovar, J. B. Green Jr., F.-Y. Zhang, *Int. J. Hydrogen Energy* **2018**, 43 (31), 14618–14628.

[33] T. Schuler, J. M. Ciccone, B. Krentscher, F. Marone, C. Peter, T. J. Schmidt, F. N. Büchi, *Adv. Energy Mater.* **2020**, 10, 1903216.

[34] P. Lettenmeier, R. Wang, R. Abouatallah, B. Saruhan, O. Freitag, P. Gazdzicki, T. Morawietz, R. Hiesgen, A. S. Gago, K. A. Friedrich, *Sci. Rep.* **2017**, **7**, 44035.

[35] P. Lettenmeier, R. Wang, R. Abouatallah, S. Helmly, T. Morawietz, R. Hiesgen, S. Kolb, F. Burggraf, J. Kallo, A. S. Gago, K. A. Friedrich, *Electrochim. Acta* **2016**, 210, 502–511.

[36] F. J. Hackemüller, E. Borgardt, O. Panchenko, M. Müller, M. Bram, *Adv. Eng. Mater.* **2019**, 21, 1801201.

[37] K. E. Ayers, J. N. Renner, N. Danilovic, J. X. Wang, Y. Zhang, R. Maric, H. Yu, *Catal. Today* **2016**, 262, 121–132.

[38] S. Siracusano, S. Trocino, N. Briguglio, V. Baglio, A. S. Aricó, *Materials* **2018**, 11 (8), 1368.

[39] C. Rozain, E. Mayousse, N. Guilleta, P. Millet, *Applied Catalysis B: Environmental*, **2016** 182, 123 – 131.

[40] M. Eikerling, A. A. Kornyshev, *J. Electroanal. Chem.* **1999**, 475 (2), 107-123.

[41] J. K. Lee, CH. Lee, K. F. Fahy, P. J. Kim, J. M. LaManna, E. Baltic, D. L. Jacobson, D. S. Hussey, S. Stiber, A. S. Gago, K. A. Friedrich, A. Bazylak, *Energy Convers. Manag.* **2020**, 226, 113545.

[42] H. Ito, T. Maeda, A. Nakano, A. Kato, T. Yoshida, *Electrochim. Acta* **2013**, 100, 242-248.

[43] G. Schmidt, M. Suermann, B. Bensmann, R. Hanke-Rauschenbach, I. Neuweiler, *J. Electrochem. Soc.* **2020**, 167, 114511.

[44] J. K. Lee, CH. Lee, A. Bazylak, *J. Power Sources* **2019**, 437, 226910.

[45] J. K. Lee, A. Bazylak, *J. Electrochem. Soc.* **2020**, 167, 013541.

[46] J. C. Garcia-Navarro, M. Schulze, K. A. Friedrich, *ACS Sustainable Chem. Eng.* **2019**, 7 (1), 1600-1610.

[47] G. Tsotridis, JRC validated methods, reference methods and measurements report – EU Harmonised Polarisation Curve Test Method for Low Temperature Water Electrolysis, *Joint Research Center (JRC)* **2018**.

[48] T. Malkow, A. Pilenga, G. Tsotridis, JRC validated methods, reference methods and measurements report – EU harmonised test procedure: electrochemical impedance spectroscopy for water electrolysis cells, *Joint Research Center (JRC)* **2018**.

[49] F. J. Wirkert, J. Roth, U. W. Rost, M. Brodmann, *Int. J. Smart Grid Clean Energy* **2017**, 6 (3), 171-176.

[50] F. J. Wirkert, J. Roth, S. Jagalski, P. Neuhaus, U. Rost, M. Brodmann, *Int. J. Hydrogen Energy* **2020**, 45 (2), 1226-1235.

[51] J. Gostick, M. Aghighi, J. Hinebaugh, T. Tranter, M. A. Hoeh, H. Day, B. Spellacy, M. H. Sharqawy, A. Bazylak, A. Burns, W. Lehnert, A. Putz, *Comput. Sci. Eng.* **2016**, 18 (4), 60-74.

[52] J. T. Gostick, M. A. Ioannidis, M. W. Fowler, M. D. Pritzker, *J. Power Sources* **2007**, 173 (1), 277-290.

[53] S. Bryant, S. Blunt, *Phys. Rev. A* **1992**, 46 (4), 2004-2011.

[54] CH. Lee, B. Zhao, R. Abouatallah, R. Wang, A. Bazylak, *Phys. Rev. Applied* **2019**, 11, 054029-1.

[55] CH. Lee, R. Banerjee, N. Ge, J. K. Lee, B. Zhao, E. Baltic, J. M. LaManna, D. S. Hussey, D. L. Jacobson, R. Abouatallah, R. Wang, A. Bazylak, *Electrochim. Acta* **2018**, 279, 91-98.

1

Table of contents (TOC)

Novel porous transport layers for proton exchange membrane water electrolyzers that allow operation at extreme conditions of current density, temperature and pressure. The electrolyzer is thus far more efficient than the state of art resulting in lowering the cost of hydrogen produced by renewables.

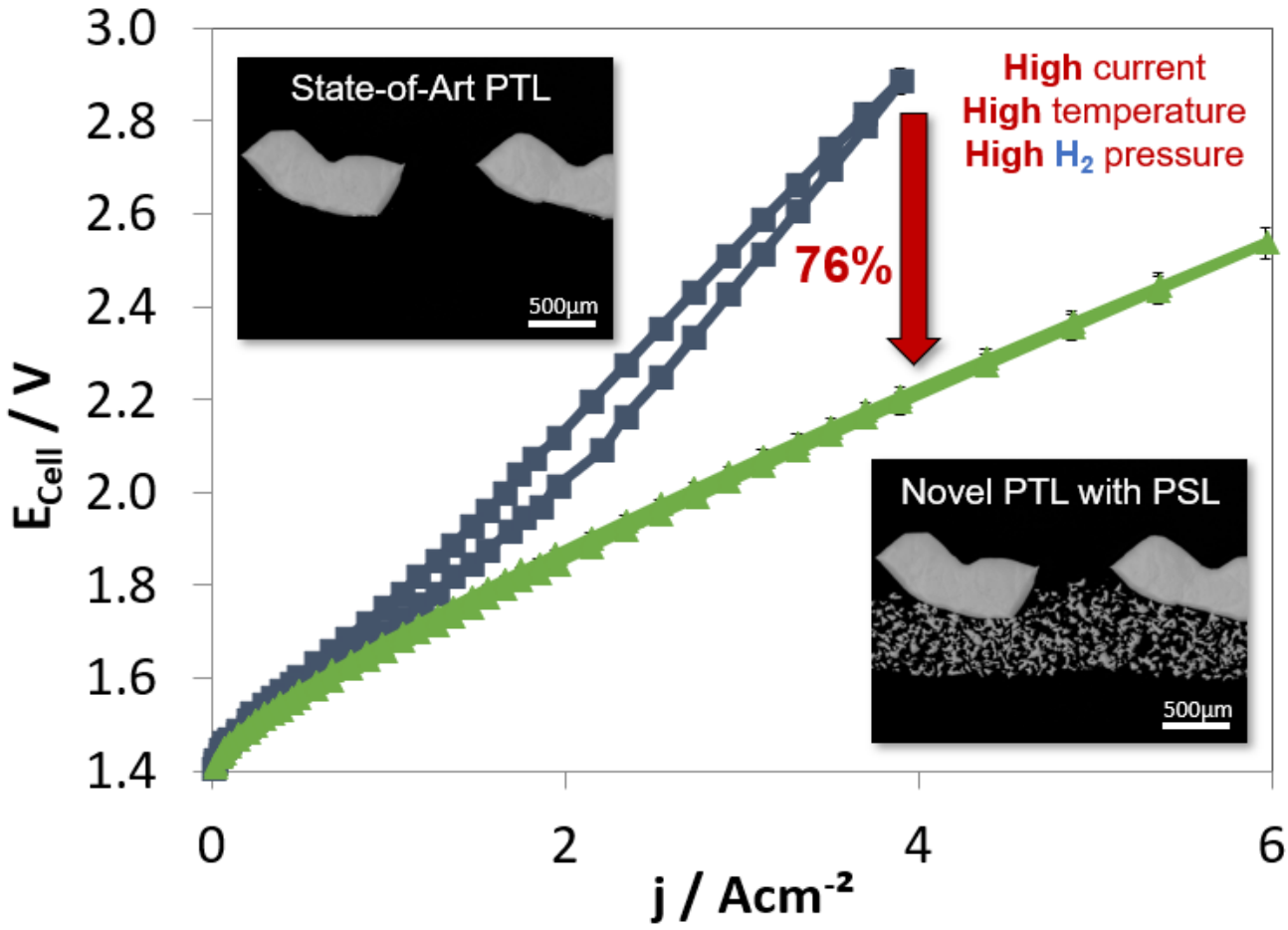

Abbreviations

H_2	hydrogen
PEMWE	proton exchange membrane water electrolysis
PTL	porous transport layer
CO_2	Carbon dioxide
AWE	alkaline water electrolysis
SoA	state-of-art
MEA	membrane electrode assembly
BPP	bipolar plates
PSL	porous sintered layer
SP	small pores
MFP	mean flow pore
LP	large pores
ICR	interfacial contact resistance
EIS	electrochemical impedance spectroscopy
HER	hydrogen evolution reaction
OER	oxygen evolution reaction
MTL	mass transport loss
CAPEX	Capital expenditures
PEEK	Polyetheretherketone